ELSEVIER

1 August 1995

OPTICS COMMUNICATIONS

Optics Communications 118 (1995) 619–636

Full length article

Application of the parabolic wave equation to X-ray diffraction optics

Yuri V. Kopylov [a], Alexei V. Popov [a], Alexander V. Vinogradov [b,*]

[a] *Institute of Terrestrial Magnetism, Ionosphere and Radio Wave Propagation, Russian Academy of Sciences, 142092 Troitsk, Moscow region, Russia*

[b] *Lebedev Physics Institute, Russian Academy of Sciences, 53 Leniskiy pr., 117924 Moscow, Russia*

Received 22 July 1994; revised version received 20 February 1995

Abstract

A new computational approach is suggested to the analysis of imaging properties of realistic X-ray Fresnel zone plates with high aspect ratio. Its mathematical basis is the parabolic wave equation (PWE) describing diffraction inside the zone plate body as well as wave propagation and focusing throughout the optical system. A finite-difference method is used for solving PWE in a truncated free-space domain with a perfectly transparent artificial boundary. The results of global wave field calculation are visualized by means of color graphics. Numerical estimates of resolution, diffraction efficiency and field of view enables one to compare imaging performance of realistic X-ray zone plates with an idealized plane Fresnel diffraction lens.

1. Introduction

X-ray imaging optics is making an impressive breakthrough towards higher resolution and efficiency. The two competitive approaches in these efforts are reflective and diffractive optical systems. The prospects of diffractive optics are mainly associated with design and manufacturing of high resolution and efficient Fresnel zone plates. An adequate wave theory of this fine multiscale object is still to be developed.

A great number of publications on the wave theory of Fresnel zone plates is summarized in Refs. [1,2]. They are mainly restricted to treating a zone plate as plane amplitude or phase screen. This approximation is not valid for actually high resolution and efficient zone plates which necessarily must be optically thick and having high aspect ratio (thickness over the zone width). In fact, to achieve a considerable amplitude or phase contrast one have to meet the following condition

$$b \geq \frac{\lambda}{|\epsilon - 1|} \tag{1}$$

* To whom the correspondence is to be addressed.

SSDI 0030-4018(95)00295-2

where λ is the wavelength, ϵ is the complex dielectric permittivity of the material forming the zone plate and b is its thickness. It is desirable and in principle possible to get the resolution about λ; however, it implies the width of the outermost zone Δ to be of the same order of magnitude [1]. Therefore, the aspect ratio

$$\frac{b}{\Delta} \geq \frac{1}{\epsilon - 1} \gg 1 \tag{2}$$

proves to be great and increasing towards the short-wavelength part of the X-ray spectral range.

Recently, in view of Eqs. (1), (2), a number of papers appeared considering realistic zone plate models beyond the frames of the plane screen Kirchhoff theory [3–5]. All of them use semi-analytical approaches based on specific models of the scattering object and sometimes involve radical approximations to simplify calculations. For example, in Ref. [5] an analytical method for the calculation of diffraction efficiency is given which is applicable to a wide class of thick zone plates. However, it is difficult to obtain on this way the detailed information about the global wave field structure and to get a reliable quantitative estimations of resolution and field of view for a realistic zone plate.

On the other hand, straightforward numerical methods of solving Maxwell's equations are extremely time consuming due to high ratio of all the geometrical scales (zone plate radius and thickness, focal length) to the wavelength λ.

We suggest an alternative computational approach based on the parabolic wave equation (PWE) [6]. It is applicable because the permittivity ϵ of all materials in X-ray range only slightly differs from its free-space value: $|\epsilon - 1| \ll 1$. Physically, this causes that all diffraction processes in an X-ray optical element have unidirectional and almost paraxial character. As point of fact, here we deal rather not with diffraction but with a wave propagation problem in a multiscale nonuniform medium composed of weak dielectric elements. The parabolic equation method has proven to be a very efficient computational tool for such problems. Using PWE crucially reduces computational time and permits to simulate numerically not only various types of Fresnel zone plates but many other elements and systems of X-ray transmission optics.

2. Parabolic wave equation (PWE)

The Leontovich-Fock parabolic wave equation has become a classical approximate approach to radio wave propagation [6] and underwater acoustics [7]. A variety of its modifications has been used in diffraction theory [8–10] and nonlinear optics [11]. Recently, an extensive use of the PWE takes place in many branches of computational electromagnetics which was anticipated earlier by Malyuzhinets [8]. We believe that X-ray imaging optics will become a new important application of this well-proven and efficient method because most of optical schemes work with paraxial wave beams and all the materials are almost transparent in this spectral region.

Let us remind how the parabolic approximation can be derived from the exact wave theory. Consider an elementary plane wave

$$E_{pq}(x, y, z) = \exp(\mathrm{i}\boldsymbol{kr}) \tag{3}$$

in free space ($\epsilon \equiv 1$). If the wave vector $\boldsymbol{k} = (p, q, \sqrt{k^2 - p^2 - q^2})$ makes a small angle $\beta = \sin^{-1}(\sqrt{p^2+q^2}/k)$ with the z-axis one can expand the exponent in powers of $\sin\beta$:

$$\sqrt{k^2 - p^2 - q^2} = k - \frac{p^2 + q^2}{2k} - \frac{(p^2 + q^2)^2}{8k^3} + \ldots \tag{4}$$

Neglecting all but the first two terms in the right-hands part leads to the following approximation

$$E_{pq}(x,y,z) = u_{pq}(x,y,z)\exp(ikz)\,, \quad u_{pq}(x,y,z) = \exp\left[i\left(px+qy-\frac{p^2+q^2}{2k}z\right)\right]. \tag{5}$$

By differentiating with respect to x, y and z one can see that an arbitrary slowly varying superposition

$$u(x,y,z) = \iint F(p,q)u_{pq}(x,y,z)\,dp\,dq \tag{6}$$

satisfies the Schrödinger type PWE

$$2ik\frac{\partial u}{\partial z} + \Delta u = 0, \qquad \Delta = \frac{\partial^2}{\partial x^2} + \frac{\partial^2}{\partial y^2}\,. \tag{7}$$

The validity condition of the approximation (4) imposes a limitation upon the maximum distance

$$z_{\max} \ll 4\lambda \sin^{-4}\beta\,, \tag{8}$$

where $\lambda = 2\pi/k$ is the wavelength. If the wave field is to be calculated at greater ranges $z > z_{\max}$, one of the long-range, wide-angle modifications of the PWE can be used [12–14]. The exact Green formula also can be used in free space to remove the restriction (8) on the maximum distance $z_{\max}$.

It is well known that, in the problem of diffraction by plane screens (e.g. a thin zone plate), the parabolic approximation is equivalent to the simplified Fresnel-Kirchhoff diffraction theory. In fact, any solution of (7) can be expressed for $z > 0$ in terms of its initial values over the aperture A in $z = 0$ plane:

$$u(x,y,z) = \iint_A u(x',y',0)\,G(x-x',y-y',z)\,dx'\,dy'\,. \tag{9}$$

Here, the Green function

$$G(x-x',y-y',z) = \frac{k}{2\pi i z}\exp\left(ik\frac{(x-x')^2+(y-y')^2}{2z}\right) \tag{10}$$

represents asymptotically a spherical wave, and (9) is nothing but a paraxial approximation of the Kirchhoff integral

$$E(x,y,z) = \frac{k}{2\pi i}\iint_A E(x',y',0)\frac{\exp(ikR)}{R}\,dx'\,dy'\,, \quad R = \sqrt{(x-x')^2+(y-y')^2+z^2}\,. \tag{11}$$

An important advantage of the parabolic equation method compared with Kirchhoff theory is that it can be easily extended upon the case of a weak nonuniform medium with complex dielectric permittivity $\epsilon = 1+\alpha(x,y,z)$, $|\alpha| \ll 1$. Substitution of the paraxial Ansatz

$$E(x,y,z) = u(x,y,z)\exp(ikz) \tag{12}$$

into the wave equation

$$E_{xx} + E_{yy} + E_{zz} + k^2\epsilon(x,y,z)E = 0 \tag{13}$$

and neglecting the second derivative of the slow amplitude u_{zz} yield the following PWE

$$2ik\frac{\partial u}{\partial z} + \Delta_\perp u + k^2\alpha(x,y,z)u = 0\,. \tag{14}$$

Being an obvious generalization of the parabolic equation (7), it describes adequately the main diffraction phenomena ("transversal diffusion" [8]) in the nonuniform dielectric medium as well as the free-space propagation and focusing outside the optical elements. Formally, the applicability conditions of the PWE (14) can be obtained by putting $\alpha(x,y,z) = \tilde{\alpha}(x/a, y/a, z/b)$ where a and b are characteristic scales of transversal and longitudinal nonuniformity of the dielectric permittivity (for a Fresnel zone plate, a is the minimum zone width: $a \approx dr_N = r_N - r_{N-1} \approx \frac{1}{2}(\lambda f/N)^{1/2}$ [1], and b is the zone plate thickness). Estimation of the neglected terms yields:

$$kb|\alpha| \leq 1, \quad ka^2/b \geq 1 . \tag{15}$$

These conditions are usually met for X-ray optical elements. In practice, however, the main averaged features of the wave field can be described correctly even under less restrictive assumptions.

If the Fresnel parameter ka^2/b proves to be large, it is possible to omit in Eq. (14) the diffusion term $\Delta_\perp u$ which leads to the plane screen approximation

$$u(x,y,b) = u(x,y,0)\exp\left(\mathrm{i}\frac{k}{2}\int_0^b \alpha(x,y,z)\,\mathrm{d}z\right) \equiv T(x,y)\ u(x,y,0) , \tag{16}$$

supplying initial values $u(x,y,b)$ for the Fresnel-Kirchhoff integral (9). However, as X-ray zone plates use to have high aspect ratio b/a and large number of zones N, the complete PWE (14) is to be used to accurately take into account the diffraction processes inside the plate body.

3. Computational aspects of the PWE

Transition from rigorous wave theory to the transversal diffusion approximation leads to the change of kind of the differential equations and to a new formulation of the boundary value problem. In contrast to the elliptic wave equation, the PWE (14) describes the evolution of the wave amplitude in process of almost unidirectional propagation along the optical axis. Physically, it means neglecting the backward reflections from the interfaces and inaccurate description of the waves diffracted into large off-axis angles (such approximation is adequate for the variations of the refraction index are supposed to be small which limits the intensity of wide-angle diffraction).

For the parabolic equation (14), the Cauchy problem with a given initial distribution $u(x,y,0) = u_0(x,y)$ is correctly posed if some radiation condition is added excluding spurious waves coming from $y = \pm\infty$. Analytically, the simplest way is to demand that the solution must be bounded at infinity when an arbitrarily small absorption $\mathrm{Im}\,k > 0$ is introduced (Malyuzhinets' "principle of extinguishing" [8]). Unfortunately, the extinguishing condition is difficult to implement in the process of numerical solution of the problem which demands truncation of the spatial domain. It makes one to seek a way of transferring the radiation condition from infinity to a certain finite surface surrounding all the sources and diffractive elements. Since any spurious reflection from this artificial boundary would change the wave field structure, such boundary condition has to provide full transparency for arbitrary radiation coming from inside.

In a model two-dimensional case, an exact form of the transparency condition

$$\frac{\partial u}{\partial x}(x,\pm A) = \mp\exp(-\mathrm{i}\pi/4)\sqrt{2k\frac{\partial}{\partial z}}\,u(x,\pm A) \tag{17}$$

has been found in Refs. [15,16]. It can be derived formally by factorization of the differential operator

$$2\mathrm{i}k\frac{\partial}{\partial z} + \frac{\partial^2}{\partial x^2} = \left(\frac{\partial}{\partial x} + \exp(-\mathrm{i}\pi/4)\sqrt{2k\frac{\partial}{\partial z}}\right)\left(\frac{\partial}{\partial x} - \exp(-\mathrm{i}\pi/4)\sqrt{2k\frac{\partial}{\partial z}}\right) \tag{18}$$

corresponding to the free-space version (7) of the PWE; here, the symbol of fractal derivative

$$\sqrt{\frac{\partial}{\partial z}}\,u(z) = \frac{1}{\sqrt{\pi}}\frac{\partial}{\partial z}\int_0^z u(\zeta)\,\frac{\mathrm{d}\zeta}{\sqrt{z-\zeta}} \tag{19}$$

is used to describe the nonlocal surface admittance.

Quite similarly, in three dimensions the radiation condition can be transferred from infinity to an arbitrary cylindric surface $r = A$ surrounding all the dielectric elements. In fact, if $\alpha(x, y, z)$ and $u_0(x, y)$ vanish for $r = \sqrt{x^2 + y^2} > A$, in this region an arbitrary solution $u(r, \varphi, z)$ of the PWE (14) satisfying the radiation condition can be expressed analytically in terms of its boundary values $u(A, \varphi, z)$:

$$u(r,\varphi,z) = \frac{1}{2\pi}\frac{\partial}{\partial z}\int_0^z\int_0^{2\pi} u(A,\psi,\zeta)\,L(r,\varphi-\psi,z-\zeta)\,\mathrm{d}\zeta\,\mathrm{d}\psi \tag{20}$$

for $r > A$. Here,

$$L(r,\varphi,z) = \frac{1}{2\pi\mathrm{i}}\sum_{m=-\infty}^{\infty}\exp(\mathrm{i}m\varphi)\int_{c-\mathrm{i}\infty}^{c+\mathrm{i}\infty}\frac{H_m^{(1)}(r\sqrt{2\mathrm{i}kp})}{H_m^{(1)}(A\sqrt{2\mathrm{i}kp})}\exp(pz)\,\frac{\mathrm{d}p}{p}\,, \tag{21}$$

and $H_m^{(1)}(t)$ is the Hankel function of the first kind. Calculating the normal derivative yields the following integral relation

$$\frac{\partial u}{\partial r}(A,\varphi,z) = \frac{1}{2\pi}\frac{\partial}{\partial z}\int_0^z\int_0^{2\pi} u(A,\psi,\zeta)\,K(\varphi-\psi,z-\zeta)\,\mathrm{d}\zeta\,\mathrm{d}\psi\,, \tag{22}$$

with

$$K(\varphi,z) = \exp(-\mathrm{i}\pi/4)\,\frac{\sqrt{k}}{\pi\sqrt{2}}\sum_{m=-\infty}^{\infty}\exp(\mathrm{i}m\varphi)\int_{c-\mathrm{i}\infty}^{c+\mathrm{i}\infty}\frac{H_m^{(1)\prime}(A\sqrt{2\mathrm{i}kp})}{H_m^{(1)}(A\sqrt{2\mathrm{i}kp})}\exp(pz)\,\frac{\mathrm{d}p}{\sqrt{p}}\,. \tag{23}$$

Due to continuity of the solution, it can serve as a nonlocal boundary condition for the numerical integration of the parabolic equation (14) inside the cylinder $r < A$.

In the most interesting axial symmetric case, only the term $m = 0$ remains in Eqs. (21) and (23). Moreover, as usually the integration region is very wide compared with the wavelength ($kA \gg 1$), the Hankel function can be replaced by its far-field asymptotic expression $H_m^{(1)}(t) \sim -\sqrt{2k/\pi t}\exp[\mathrm{i}(t-\pi/4)]$. Then the zero-order term in (23) can be calculated explicitly:

$$K_0(z) \approx -\exp(-\mathrm{i}\pi/4)\sqrt{2k/\pi z}\,, \tag{24}$$

which reduces the boundary condition (20) to the form

$$\frac{\partial u}{\partial r}(A,z) = -\exp(-\mathrm{i}\pi/4)\sqrt{\frac{2k}{\pi}}\frac{\partial}{\partial z}\int_0^z u(A,\zeta)\,\frac{\mathrm{d}\zeta}{\sqrt{z-\zeta}} \tag{25}$$

coinciding with Eq. (17). Its numerical implementation [15] provides, with high accuracy, full transparency of the artificial boundary $r = A$ in all practical examples.

Many aspects of the numerical solution of the parabolic equation have been thoroughly studied (e.g. Refs. [17–21]). Confining ourselves to the axial symmetric case, we use the following six-point implicit finite-difference scheme

$$2ik\frac{u_m^{n+1}-u_m^n}{\tau}+\frac{u_{m+1}^{n+1}-2u_m^{n+1}+u_{m-1}^{n+1}+u_{m-1}^n-2u_m^n+u_{m-1}^n}{2h^2}$$
$$+\frac{u_{m+1}^{n+1}-u_{m-1}^{n+1}+u_{m+1}^n-u_{m-1}^n}{4mh^2}+k^2\alpha_m^{n+1/2}\frac{u_m^{n+1}+u_m^n}{2}=0, \tag{26}$$

reducing the PWE (14) to a three-diagonal set of linear algebraic equations. Here, τ and h are the mesh steps in z and r directions, and $u_m^n \approx u(n\tau, mh)$. As the coefficient $\alpha(r,z)=\epsilon-1$ has discontinuities at the interfaces, a better performance is shown by the modified scheme where coefficient $\alpha_m^{n+1/2}$ is replaced by its weighted average value

$$\tilde{\alpha}_m^{n+1/2}=\frac{1}{mh^2\tau}\int_{n\tau}^{(n+1)\tau}\mathrm{d}z\int_{(m-1/2)h}^{(m-1/2)h}\alpha(r,z)r\,\mathrm{d}r \tag{27}$$

given by the integral-interpolation method [22]. The linear equations (26) written for $m=0,1,\ldots,M=A/h$, along with the finite-difference approximation of the transparency condition (25)

$$\frac{u_{M-1}^{n+1}-u_{M-1}^{n+1}}{2h}+2\sqrt{\frac{2k}{\mathrm{i}\pi\tau}}\left(u_M^{n+1}-\sum_{s=1}^{n}\gamma_s u_M^{n+1-s}\right)=0, \tag{28}$$

with

$$\gamma_s=\frac{2}{\left(\sqrt{s+1}+\sqrt{s}\right)\left(\sqrt{s}+\sqrt{s-1}\right)\left(\sqrt{s+1}+\sqrt{s-1}\right)}$$

form a complete set of equations which can be solved step by step, from n to $n+1$, by the marching method, cf. Ref. [15]. Note that the three-diagonal character of the transition matrix is an important feature of the finite-difference approach reducing the computing time compared with other methods. The energy balance law

$$\sum_{m=0}^{M}m|u_m^n|^2\le\sum_{m=0}^{M}m|u_m^0|^2 \tag{29}$$

can be proved for the equations (26) which grants convergence and stability of the computational scheme [22].

The approximation error of the finite-difference equations (26) has the order of magnitude $O(h^2+\tau^2)$. Physically, it is evident that the mesh steps h and τ must be small compared with the transversal and longitudinal scales of the dielectric element: $h\ll a$, $\tau\ll b$. In free space, to describe accurately a plane-wave solution (5) with $p\sim 2\pi/a$, the mesh steps must satisfy the following criteria

$$h\ll a,\quad \tau\ll a^2/\lambda,\quad \tau\ll a^3/\sqrt{\lambda^3 z}. \tag{30}$$

The first two conditions provide a good local approximation of the slow wave amplitude $u(r,z)$, and the third one impedes the phase error accumulation at great distances z. At the PWE applicability limit $z\sim a^4/\lambda^3$, the latter condition reduces to $\tau\ll a$ but usually the longitudinal step can be chosen much greater that the transversal one.

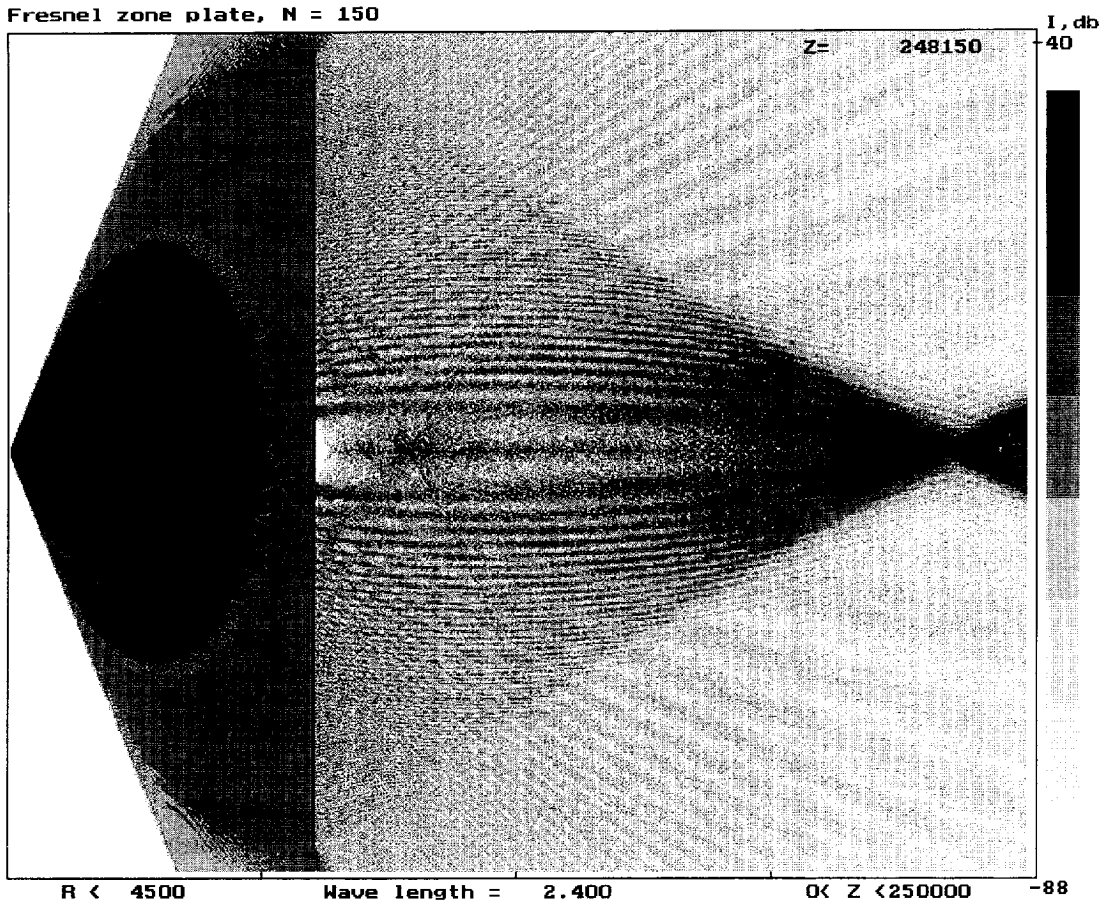

Fig. 1. Global field intensity distribution displayed in a logarithmic graded grey scale. Thin Fresnel zone plate illuminated by "point" source (a circular hole of diameter 10 nm) is placed at $z = 75$ μm; the image appears at $z \approx 225$ μm (all dimensions are given in nanometers). Parameters of the zone plate are: number of zones $N = 150$, external radius $r_N = 4.2$ μm, focal length $f = 50$ μm, wavelength $\lambda = 2.4$ nm.

A rough estimate of the computation time can be obtained by considering the total number of the mesh nodes in the region $r < A$, $z < L$:

$$MN = AL/h\tau \gg AL\lambda/a^3 . \tag{31}$$

Compared with the value AL/λ^2 for a straightforward numerical method e.g. Ref. [23], it gives an acceleration coefficient $(a/\lambda)^3$ which may reach thousands for typical applications. Estimation of CPU time based on the formula (31) shows that the parabolic equation method enables one to calculate realistic X-ray zone plates on a personal computer.

The finite-difference method of solving the PWE has some important features: it is logically simple, weakly depending on specific geometry of the diffractive elements and especially efficient for calculation of the global field distribution throughout the optical system. Such global patterns, visualized by means of color graphics, are extremely useful for understanding all the details of diffraction and focusing processes.

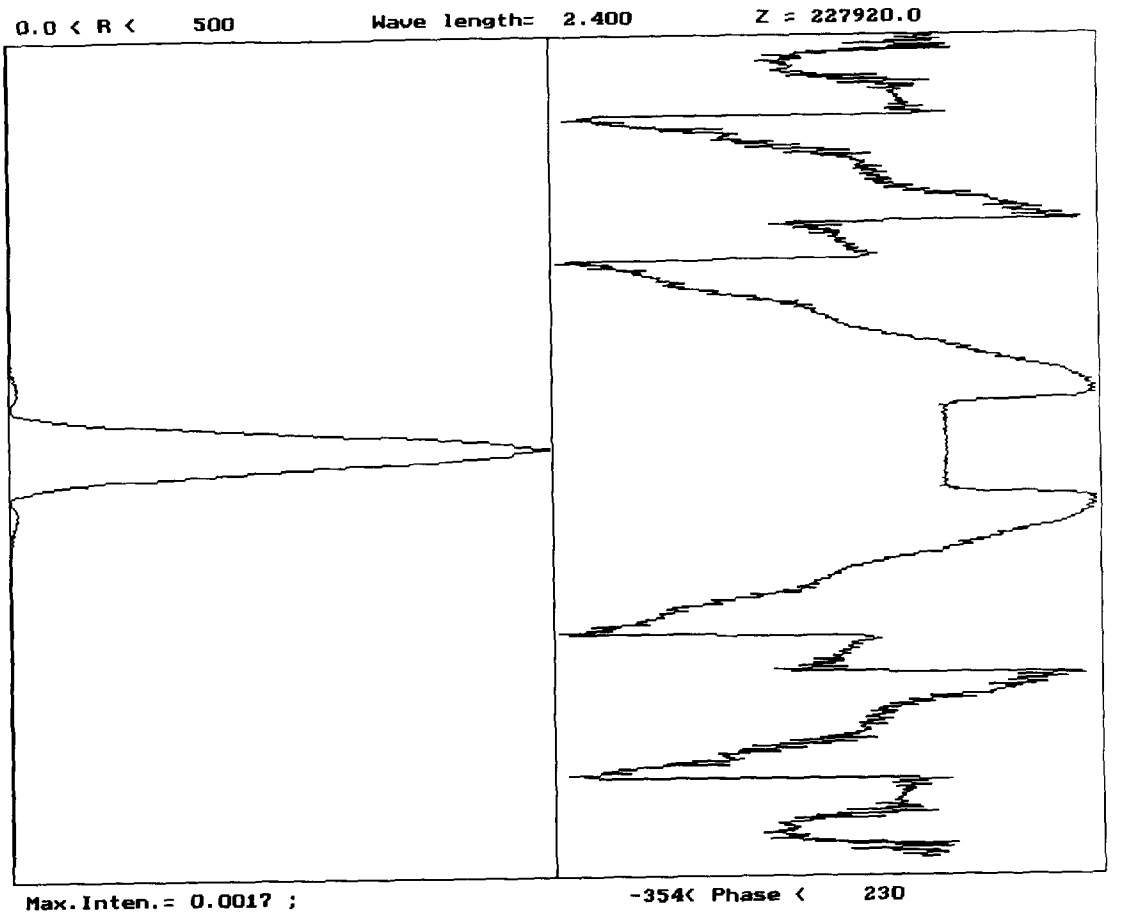

Fig. 2. Normalized radial intensity and phase distribution in image plane for the zone plate shown in Fig. 1.

4. Numerical examples

4.1. Thin zone plates

As the first useful application of the developed computational technique, we use it to analyze in detail the global wave field produced by a classical thin Fresnel zone plate. This example lies within the framework of plane screen diffraction theory and can be treated using the Fresnel-Kirchhoff approximation [24,1]. Here, the following two possibilities arise. First, for a set of annular zones, the Kirchhoff integral can be expressed in terms of Lommel functions [1]. Still these expressions are too complicated to be used for practical calculations. Secondly, straightforward numerical quadratures or more effective fast Fourier transform can be applied to calculate the diffraction integral (11). These methods are all right if the wave field in a given cross-section (e.g., focal or object plane) is to be sought. However, when one needs to investigate the spatial field distribution in a large volume containing many cross-sections, the finite-difference approach proves to be more efficient as its CPU time per point is less compared with other methods.

Below, we demonstrate a number of global field distributions which have not been published before. They contain a large amount of visual and quantitative information that is very useful to better understand the mechanisms of image formation by a Fresnel zone plate.

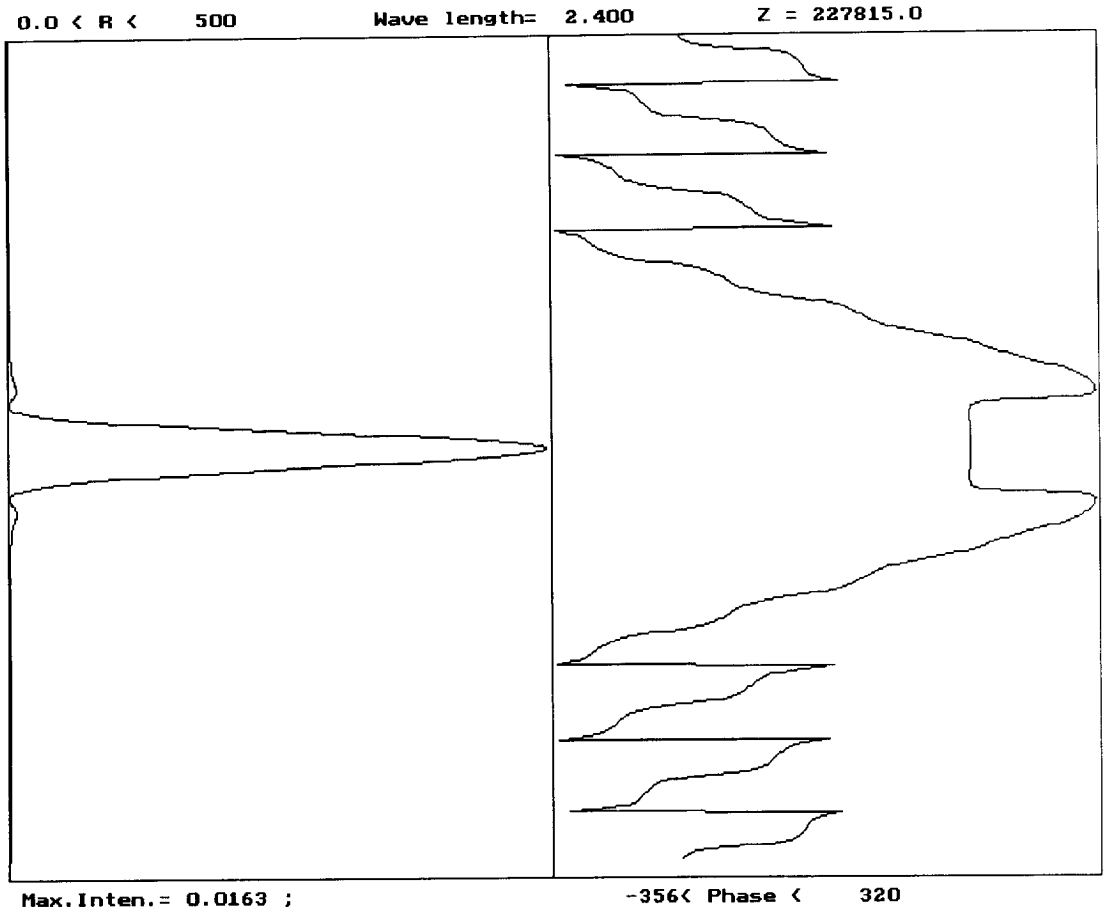

Fig. 3. Radial intensity and phase distribution in image plane for an equivalent ideal thin lens (quadratic phase screen) calculated for the geometry of Fig. 1.

In order to solve the problem of diffraction by an optically thin zone plate we use the following computational algorithm. The incident wave amplitude on the front surface $u(r,0)$ is found from an exact free-space solution of the wave equation with given radiation source. The action of the zone plate is simulated via multiplication of the input wave amplitude by the complex transmission function $T(r)$ of an equivalent plane screen (16). The resulting field serves as the initial value $u_0(r)$ for numerical solution of the PWE in a truncated free-space domain (semi-cylinder $z > 0$, $r < A$) with the perfectly transparent boundary $r = A$, see Eq. (25). The finite-difference equations (26) with corresponding nonlocal grid boundary conditions (28) are solved step by step in z direction.

We have calculated a series of global field intensity distributions produced by an amplitude Fresnel microlens composed of 75 opaque zones ($N = 150$) with

$$T(r) = \begin{cases} 0 & \text{for } r_{2n-2} < r < r_{2n-1}, \quad n = 1,\ldots,N\ , \\ 1 & \text{for } r_{2n-1} < r < r_{2n}, \quad n = 1,\ldots,N\ . \end{cases} \tag{32}$$

Several sources of illumination have been examined: point source and ring sources of different radii. By choosing the external radius $r_N = 4243$ nm we obtain the focal length $f = r_N^2/\lambda N = 50$ μm for a typical

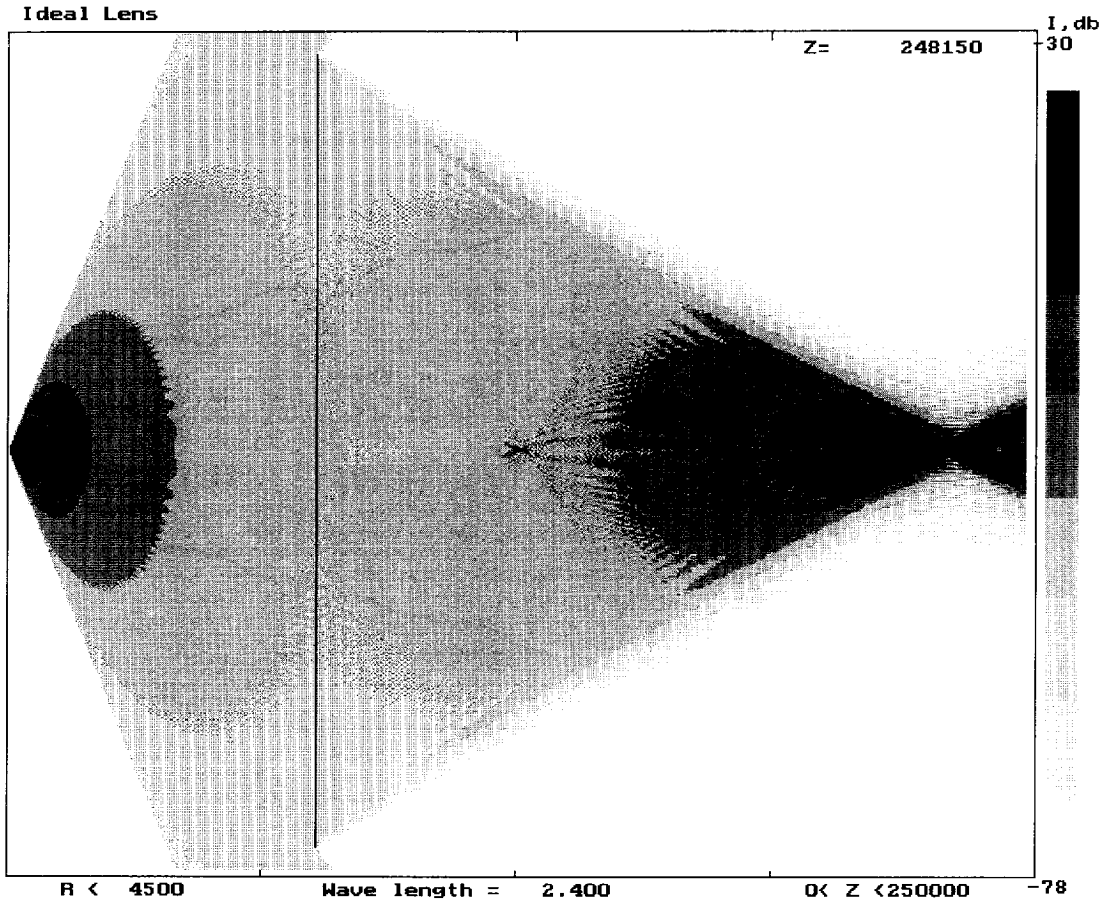

Fig. 4. Global intensity distribution for the ideal thin lens of Fig. 3.

wavelength $\lambda = 2.4$ nm in the "water window" range. The outermost zone width $dr_N = r_N/2N$ equals 14 nm, so we can expect maximum spatial resolution about $1.22dr_N \approx 17$ nm [1].

In our first model example, the ideal thin zone plate is illuminated by a "point" source placed at $Z = 75$ μm apart, so the image must be expected at $Z' = 150$ μm (actually, in order to obtain a more realistic field pattern, we substitute the point source by a circular hole of finite diameter 10 nm). The calculated field intensity distribution, displayed in Fig. 1 in a logarithmic color scale, shows a sharp focus at this point. The radial intensity distribution near the optical axis (see Fig. 2) is similar to the "point spread function" of an equivalent ideal lens

$$T(r) = \begin{cases} \exp\left(\mathrm{i}k\frac{R^2-r^2}{2f}\right), & r < R, \\ 0, & r > R, \end{cases} \tag{33}$$

(quadratic phase screen with the same external radius and focal length) calculated by the same finite-difference method and shown in Fig. 3 (the corresponding global field pattern is given in Fig. 4). The only difference is a much lower peak intensity. The ratio of these peak intensities may be used as a measure of diffraction efficiency of the zone plate. In our example, this ratio is equal to 0.1 which coincides with the theoretical estimate $1/\pi^2$ [1].

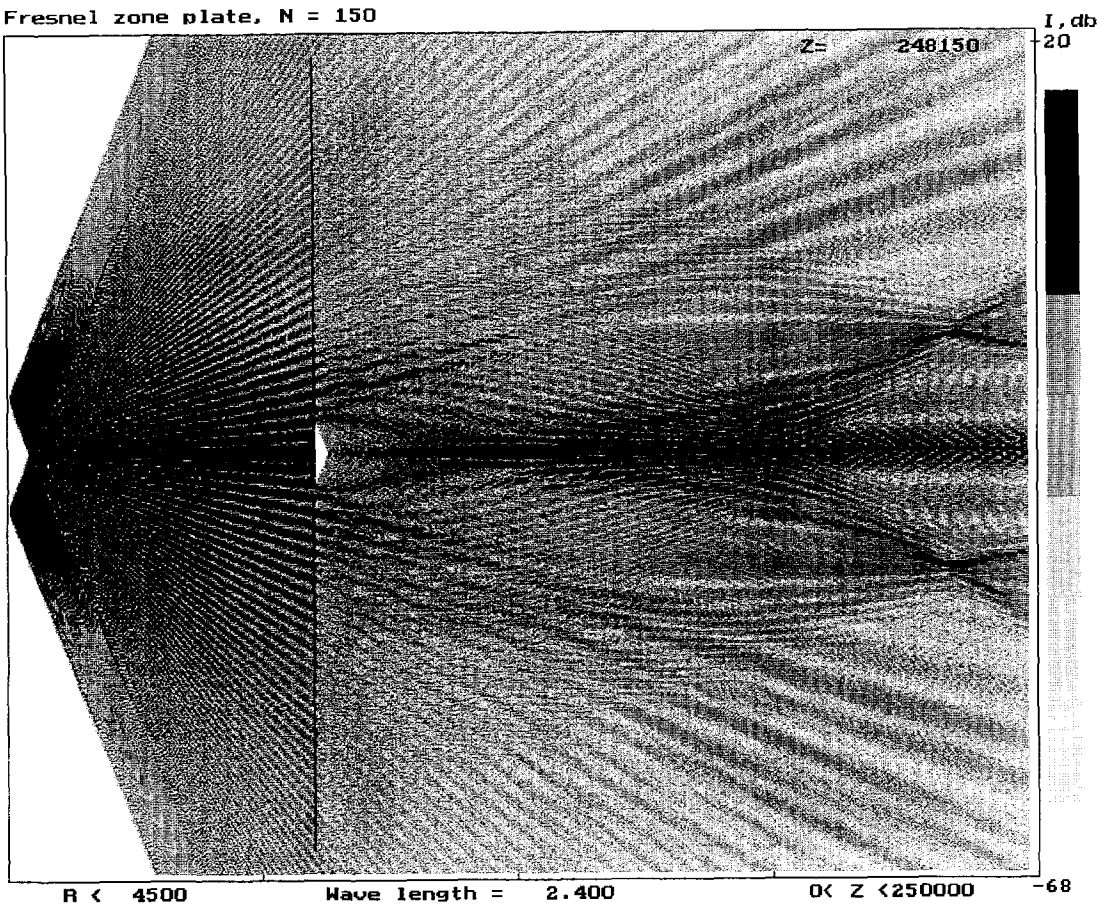

Fig. 5. Global field intensity distribution for the thin zone plate of Fig. 1 illuminated by a ring source with radius $a = 600$ nm.

The radius of the first dark ring in the image plane is about $Y' \approx 50$ nm (see Fig. 2) which gives, after dividing by magnification factor $M = Z'/Z = 2$, the value $Y \approx 25$ nm in the object plane. This agrees with the well-known Rayleigh criterion [24]

$$Y = 0.61 \frac{\lambda}{\sin\theta} = 25.9\,\text{nm}, \tag{34}$$

where $\sin\theta \approx r_N/Z = 0.0565$ is numerical aperture.

Figs. 1, 4 display many details of the diffraction patterns: edge diffraction, constructive interference near the geometric image point, higher-order foci (though the latter are formed by wide-angle wave beams, the accuracy of the PWE, according to (8), is enough to approximately describe the third-order focus seen in Fig. 1). They clearly show the difference between the fields produced by a lens and a zone plate. In the latter case, the focusing beam is sparse due to splitting by local diffraction gratings at each point of the zone plate. The undiffracted radiation and the divergent wave of minus one diffraction order, mutually interfering, produce an oscillating background clearly seen outside the main converging beam. They are responsible for the energy loss leading to the efficiency decrease.

As an example of image-forming properties of the Fresnel zone plate, we demonstrate the global wave field produced by a coherent ring source. In the parabolic approximation, it generates on the front side of the zone

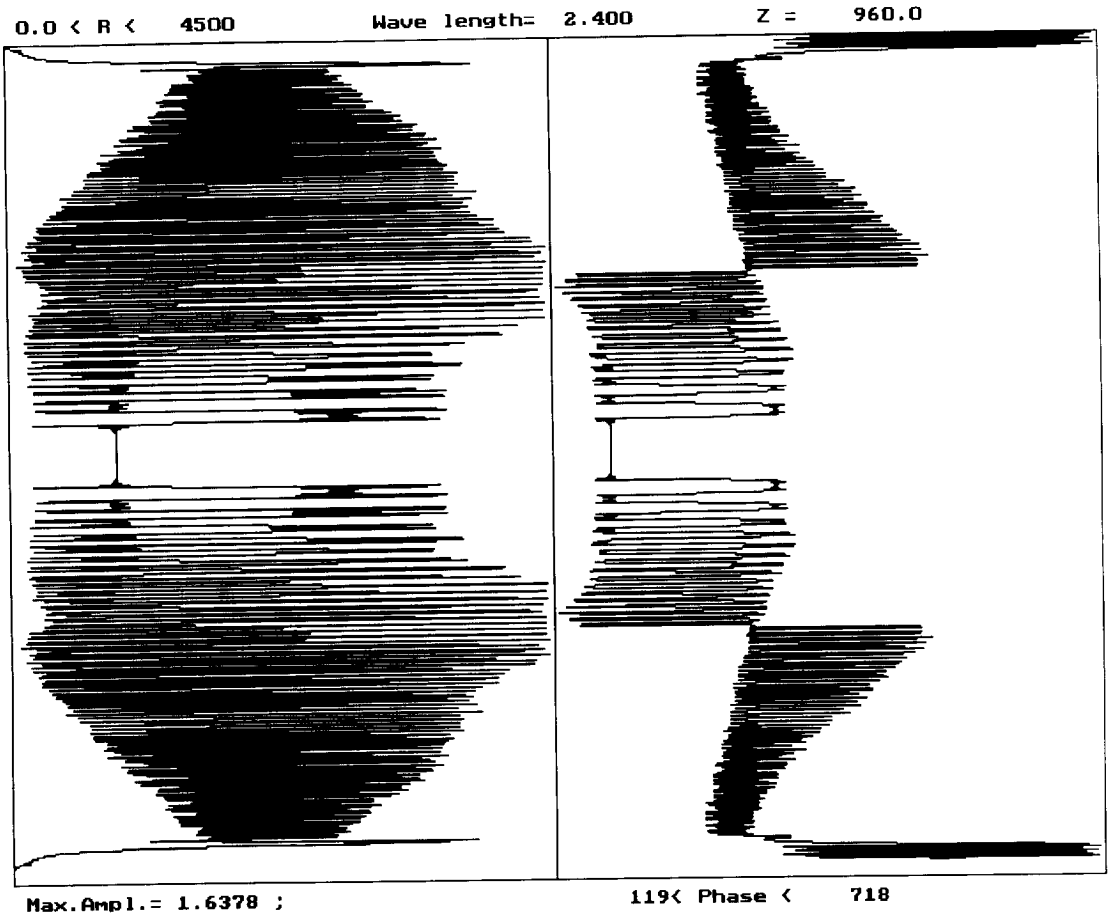

Fig. 6. Radial intensity and phase distribution on the back side of thick zone plate (Ge-vacuum, number of zones $N = 150$, external radius $r_N = 4.2$ μm, thickness $b = 460$ nm) illuminated by plane wave.

plate the field distribution close to

$$u_0(r) \approx A \exp(-ikr^2/2Z)\, J_0(kra/Z)\,. \tag{35}$$

Here, a and Z are radius and position of the ring source, and A is proportional to its amplitude. Function (35), multiplied by the stepwise transmission function of the Fresnel zone plate, has been used as an initial value for the calculations presented in Fig. 5. This example has been computed for $a = 600$ nm and $Z = 75$ μm which gives twofold magnification $M = 2$.

Looking at Fig. 5, one can easily trace the stream lines of the electromagnetic radiation forming a bright ring of radius $a' = 2a$ placed at the range $Z' = 150$ nm from the zone plate. It is obviously the diffraction image of the ring source. The bright central beam is due to constructive interference of all the diffracted rays at the optical axis. In this case, it must be considered as spurious background masking the ring image. As our calculations show, its intensity is growing up with increasing radius a faster than the image brightness. This imposes a limitation on the field of view when a coherently radiating object is to be imaged by a Fresnel zone plate.

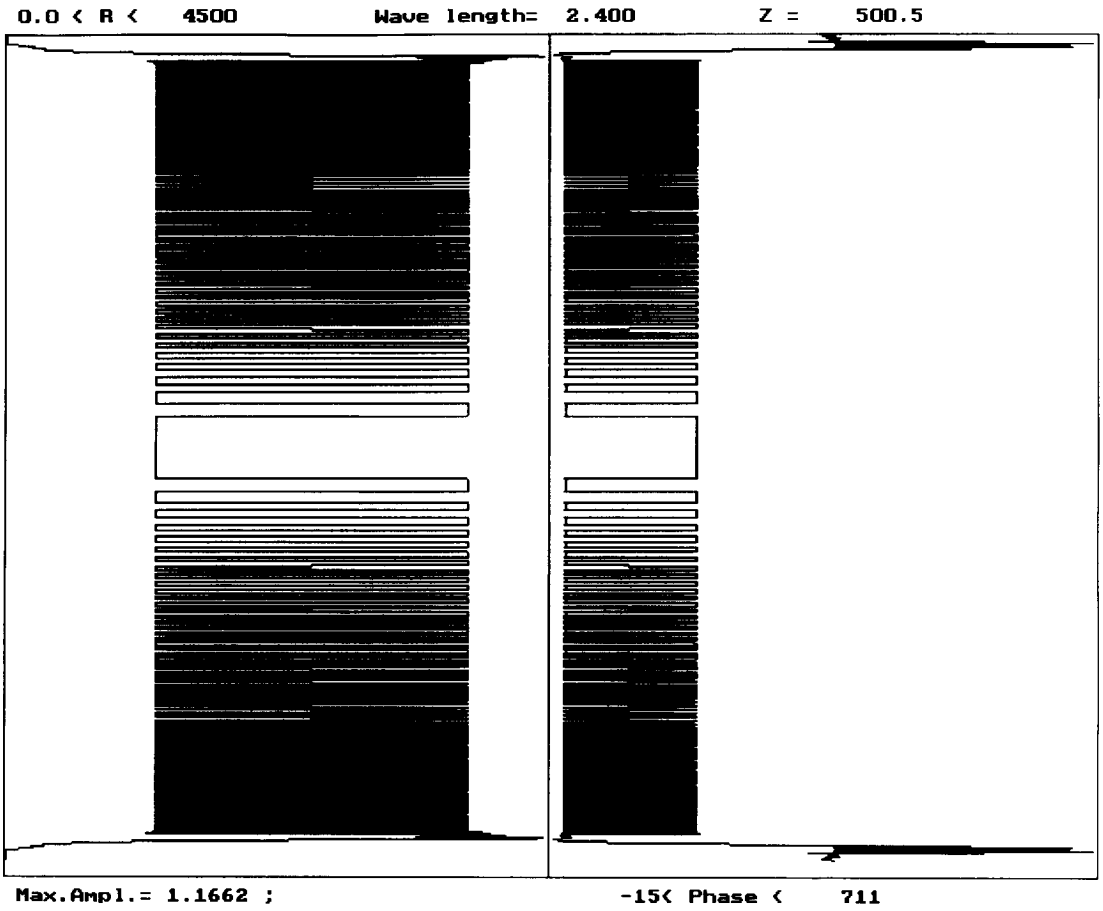

Fig. 7. Output intensity and phase distribution in the plane-screen approximation, cf. Fig. 6.

4.2. *Thick zone plates*

More interesting are the following examples related to realistic models of the optically thick Fresnel zone plates. Here, the amplitude or phase screen approximation can serve but for a very rough estimate of the zone plate transmission function. As it will be seen below, the diffraction processes essentially modify the output field distribution which may change the expected optical properties.

We have estimated numerically the performance of a series of thick Fresnel zone plates. The external radius r_N and the number of zones have been chosen coinciding with the above model examples. The optical constants of the opaque zone material (germanium) in the complex refraction index representation

$$n = \sqrt{\epsilon} = 1 - \delta + i\beta \tag{36}$$

are: $\delta = 0.0026, \beta = 0.00094$ for the chosen wavelength $\lambda = 2.4$ nm.

As the refraction and absorption factors δ and β are of the same order of magnitude, such realistic zone plate works unlike both amplitude and phase idealized Fresnel zone plates. In a rough approximation, the plane screen transmission function (16) can be used to choose its optimal thickness. After substituting $\alpha = \epsilon - 1 \approx 2(i\beta - \delta)$ into the formula (16) we get an estimate of absorption and phase shift caused by the opaque zones:

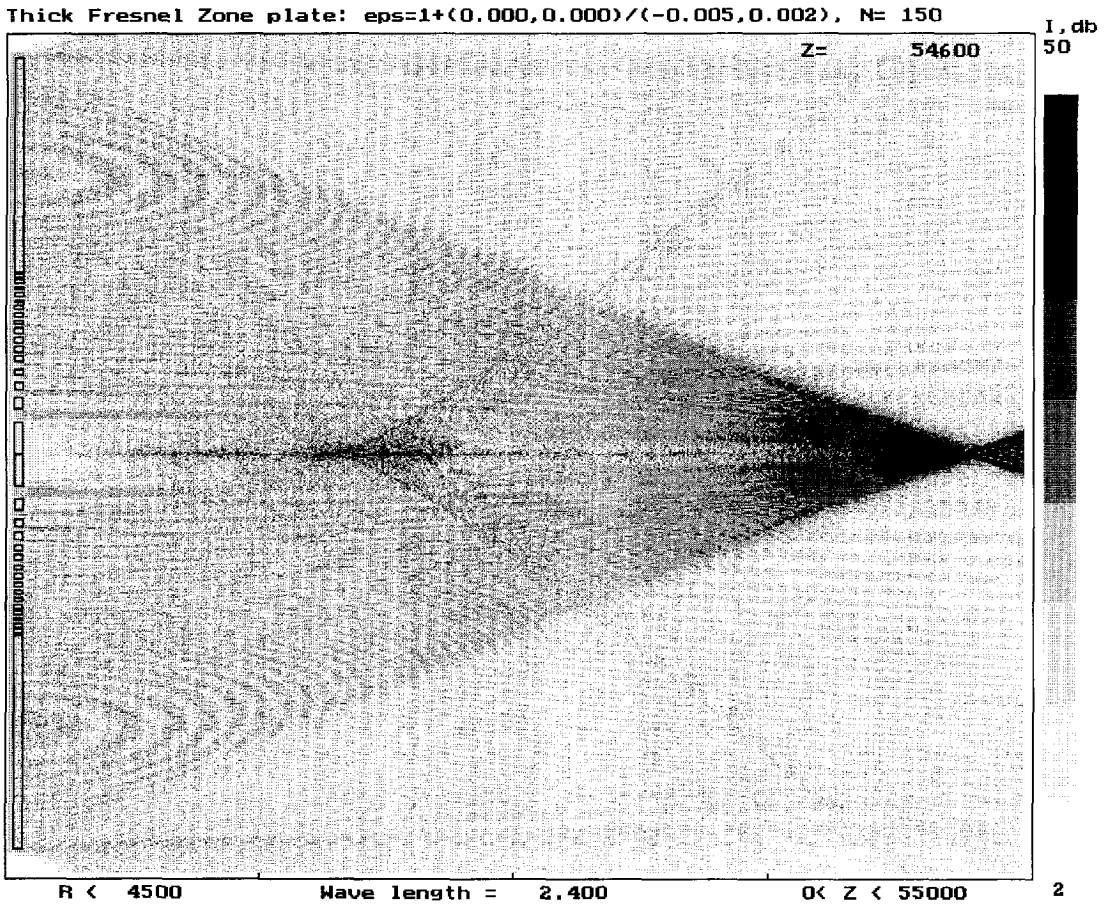

Fig. 8. Global intensity distribution for the thick zone plate of Fig. 6 illuminated by plane wave (plane-screen approximation).

$$\log|T| = -kb\beta \approx -b/400, \quad \arg T = -kb\delta \approx -\pi b/460, \tag{37}$$

where b is the zone plate thickness in nanometers.

We see that phase shift is about π for $b = 460$ nm. If it were not for absorption, this thickness would provide a very good performance close to that of an ideal Rayleigh-Wood phase zone plate [1]. For greater thicknesses, due to absorption, the amplitude contrast falls which diminishes the diffraction efficiency. A clear theory of this effect based on the plane-screen approxiamtion has been given in Ref. [25]. However, as it will be shown below, diffraction in the zone plate body modifies the output field considerably. Only numerical calculations allow to take this effect into account.

Fig. 6 shows the field distribution on the back side of the thick zone plate of the thickness $b = 460$ nm. This is a result of numerical integration of the PWE (14) inside the zone plate body. The plane incident wave has been taken in order to obtain directly the effective transmission function of the zone plate. As it is seen from Fig. 6, the output field differs considerably from the "meander" transmission function

$$T(r) = \begin{cases} \exp\left(\mathrm{i}k\frac{\alpha}{2}b\right) & \text{for } r_{2n-2} < r < r_{2n-1}, \quad n = 1, \ldots, N, \\ 1 & \text{for } r_{2n-1} < r < r_{2n}, \quad n = 1, \ldots, N, \end{cases} \tag{38}$$

predicted by the plane screen approximation (16) and shown in Fig. 7.

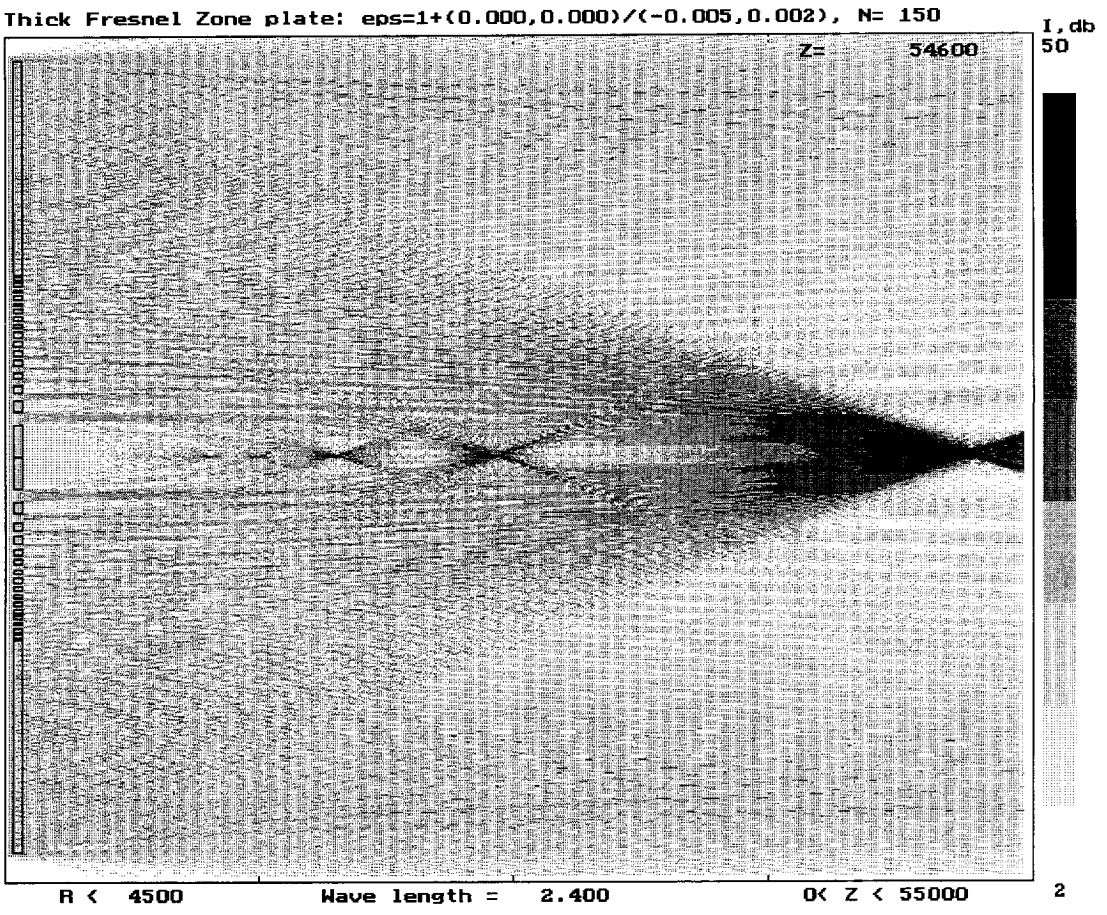

Fig. 9. Global intensity distribution for the thick zone plate of Fig. 6 illuminated by plane wave (full-wave calculation).

Figs. 8, 9 illustrate the imaging performance of this realistic Fresnel zone plates illuminated by a plane wave compared with its plane-screen model (38). It could be expected that the zone plate with optimized thickness b = 460 nm produces a brighter image than an analogous thin Fresnel lens. However, the use of plane-screen transmission function (38) can be misleading in calculation of its diffraction efficiency. The efficiencies estimated by comparison with the equivalent perfect lens (33) are 11 % for considered thick zone plate and 18 % for its plane-screen model (38). The latter estimate is in a good agreement with Kirz's formula [25]. Our full-wave calculation gives a lower value of diffraction efficiency. The discrepancy is about 7% which can be explained by rather high level of the even-order foci produced by the thick zone plate (see Figs. 9 and 10) but lost in the plane-screen approximation [25].

Our last example of the wave field produced by a ring source ($a = 200$ nm), see Fig. 11, shows that realistic zone plates with high aspect ratio $A = b/dr_N \sim 30$ retain most of the imaging properties of the classical Fresnel zone plate providing at the same time a higher diffraction efficiency.

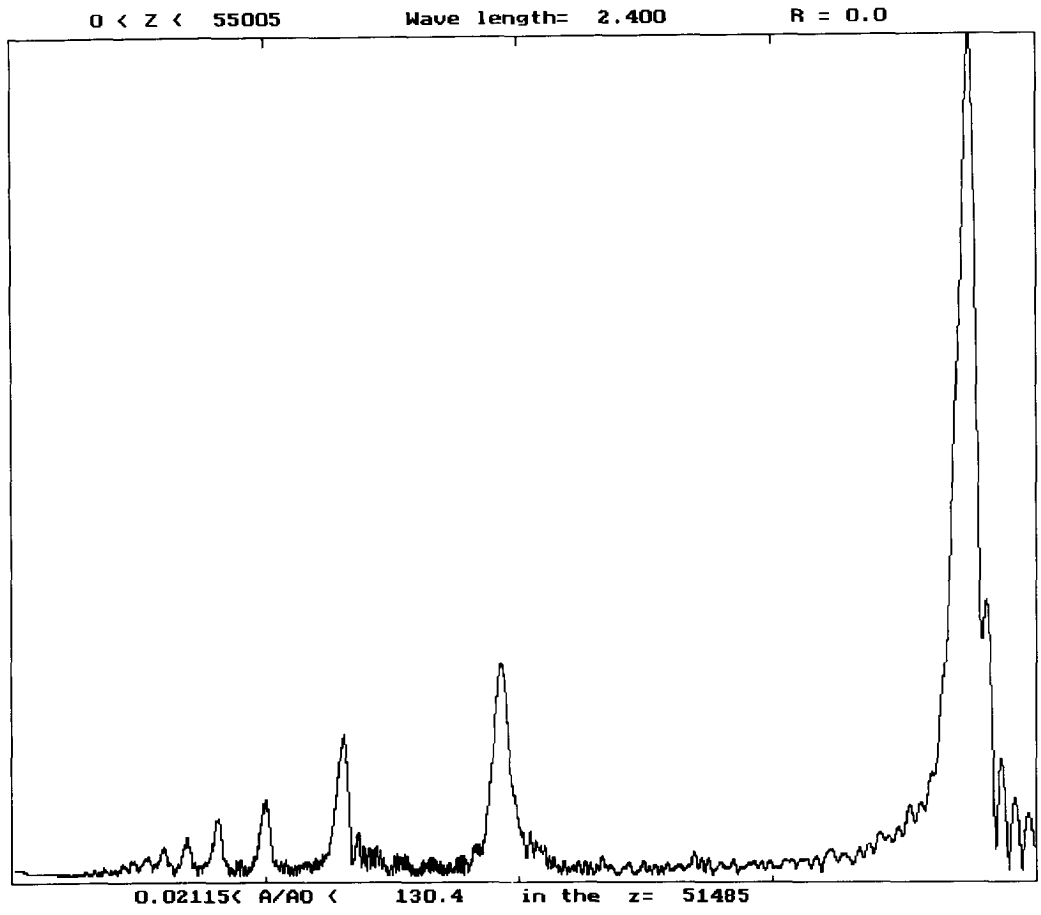

Fig. 10. Axial intensity distribution for the thick zone plate (cf Fig. 9).

5. Conclusion

A new method to calculate imaging properties of X-ray Fresnel zone plates is suggested and implemented numerically. The mathematical basis of our approach is the parabolic wave equation solved by finite differences inside the zone plate body as well as in a free space region surrounded by an artificial transparent boundary. The computational procedure allows for fast calculation and visualization of the global field distribution. Resolution, diffraction efficiency and field of view of the zone plate are easily derived from the numerical solution.

The numerical examples presented above include comparison with planar Fresnel-Kirchhoff diffraction theory and simulation of realistic high aspect ratio X-ray zone plates designed for the "water window" spectral range.

Acknowledgements

This work has been supported in part by Lawrence Berkeley Laboratory and by Grant JEH100 from the International Science Foundation and Russian Government. We are grateful to Prof. D. Attwood and Prof. G. Schmahl for fruitful and encouraging discussions.

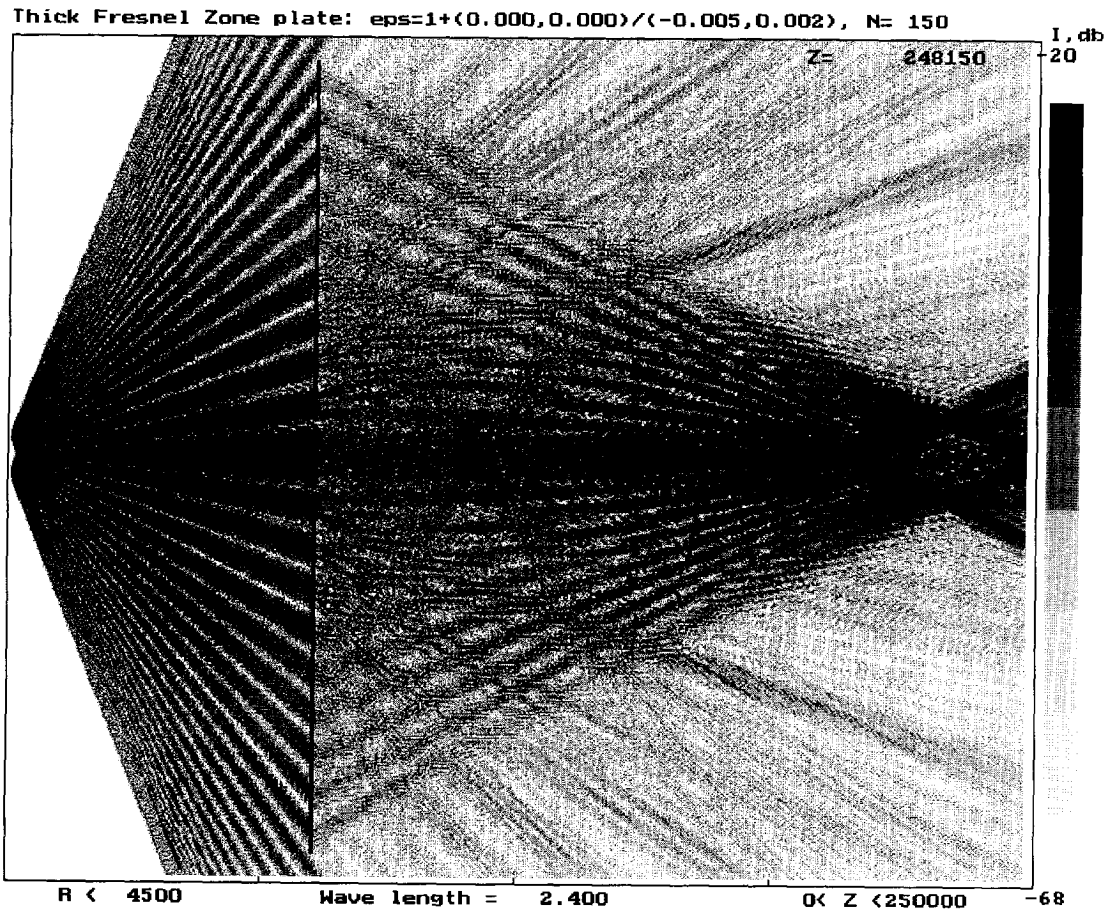

Fig. 11. Global field intensity distribution for the thick zone plate of Fig. 6 illuminated by a ring source with radius $a = 200$ nm.

References

[1] A.G. Michette, Optical systems for soft X-rays (Plenum, New York, 1986).
[2] A.G. Michette, C.J. Buckley, X-ray science and technology (Institute of Physics, Bristol, 1993)
[3] J. Maser, G. Schmahl, Optics Comm. 89 (1992) 355.
[4] A. Sammar, J.-M. Andre, J. Opt. Soc. Am. A 10 (1993) 2324.
[5] V.E. Levashov, A.V. Vinogradov, Phys. Rev. E 49, No 5 (1994).
[6] V.A. Fock. Electromagnetic diffraction and propagation problems (Pergamon, Oxford, 1965).
[7] F.D. Tappert, The parabolic approximation method, Lectures Notes in Physics, 70, in: Wave propagation and underwater acoustics, eds. J.B. Keller and J.S. Papadakis (Springer, New York, 1977) p. 224.
[8] G.D. Malyuzhinets, Soviet Physics (Uspekhi) 69 (1959) 312 (in Russian).
[9] L.A. Vainstein, Open resonators and open waveguides (in Russian), (Soviet Radio, Moscow, 1966).
[10] V.M. Babič and V.S. Buldyrev, Short-wavelength diffraction theory (asymptotic methods) (Springer, New York, 1991).
[11] V.E. Zakharov, A.B. Shabat, JETP 61 (1971) 118 (in Russian).
[12] J. Claerbout, Fundamentals of geophysical data processing with applications to petroleum prospecting (McGraw-Hill, New York, 1976).
[13] A.V. Popov, S.A. Hoziosky, J. Comp. Math. and Math. Phys. 17 (1977) 527 (in Russian).
[14] E.A. Polyansky, Method of correction of the parabolic equation solutions in a nonuniform waveguide (in Russian) (Nauka, Moscow, 1985).
[15] V.A. Baskakov, A.V. Popov, Wave Motion 14 (1991) 123.

[16] S.W. Marcus, J. Acoust. Soc. Am. 90 (1990) 391.
[17] G.D. Malyuzhinets, A.V. Popov, Yu. N. Cherkashin, On development of a numerical method in diffraction theory (in Russian), Proc. 3rd Symposium on diffraction, Nauka, Moscow, 1964, p. 176.
[18] A.V. Popov, J. Comp. Math. and Math. Phys. 8 (1968) 1140 (in Russian).
[19] G. Botseas, J.S. Papadakis,J. Acoust. Soc. Am. 70 (1981) 795.
[20] W.L. Siegmann, D. Lee, Comput. and Math. with Appl. 11 (1985) 853.
[21] V. Yu. Zavadsky, Modeling of wave processes (in Russian), (Nauka, Moscow, 1991).
[22] A.A. Samarsky, A.V. Gulin, Numerical methods (in Russian), (Nauka, Moscow, 1989).
[23] M.L. Schattenburg, K. Li, R.T. Shin, J.A. Kong, D.B. Olster, H.I. Smith, J. Vac. Sci. Technol. B 9 (1991) 3232.
[24] M. Born, E. Wolf, Principles of optics (Pergamon, Oxford, 1980).
[25] J. Kirz, J. Opt. Soc. Am. 64 (1974) 301.